Hydraulic loss analysis in a pump-turbine with special emphasis on local rigid vortex and shear

Physics of Fluids ARTICLE scitation.org/journal/phf

Hydraulic loss analysis in a pump-turbine with special emphasis on local rigid vortex and shear

Cite as: Phys. Fluids **34**, 125101 (2022); doi: 10.1063/5.0124552
Submitted: 6 September 2022 · Accepted: 8 November 2022 ·
Published Online: 1 December 2022

Zhiyi Yuan (袁志懿),[1,2] Yongxue Zhang (张永学),[1,a)] Wenbo Zhou (周文博),[1] and Cong Wang (王聪)[3]

AFFILIATIONS

[1]College of Mechanical and Transportation Engineering, China University of Petroleum, Beijing 102249, China
[2]Department of Mechanics and Maritime Sciences, Chalmers University of Technology, Gothenburg 41296, Sweden
[3]Energy Research Institute, Qilu University of Technology, Jinan 250014, China

[a)]**Author to whom correspondence should be addressed:** zhyx@cup.edu.cn

ABSTRACT

Since the pump as turbine is increasingly employed in energy storage, improving efficiency in both pump and turbine modes is required for economic benefits. This study aims to analyze vortex flow characteristics and vortex control methods in both modes to reduce hydraulic loss. In this paper, a delayed detached eddy simulation was applied in a low specific speed pump-turbine. Based on the entropy production analysis and vorticity binary decomposition in the local vortices, the results show that the local shear is the leading cause of hydraulic loss instead of the existence of vortices. The average wake loss can be 1.6 times higher than the loss in jet regions in pump mode, but there is little difference in the distribution of shear and vortices in the wake flow in turbine mode. The local loss caused by the rotor–stator interaction with a tongue effect at blade passing frequency is up to threefold over the loss without a tongue effect in both modes. Reducing shear and ratio of shear to rigid vorticity of the local vortices via modification in the volute tongue angle to suppress the tongue effect can be an effective way to decrease hydraulic loss in both modes.

I. INTRODUCTION

Pump as turbine (PAT) running in pump and turbine modes is becoming a promising solution in energy storage and grid load control for the growth of renewable energy production since changes between the power production and consumption need to be balanced.[1,2] PAT saves the cost of purchasing a turbine and is convenient to maintain. It can be used in a micro-pumped storage power system, as well as in complex systems with wind power or a photovoltaic system, especially in rural areas with a sufficient amount of space and slope.[3,4] Moreover, the high-head pump-turbine is the trend to develop to reduce the investment, which means the low specific speed pump-turbine is gaining more attention.[5] As pump-turbine efficiency is closely related to economic benefits, ensuring that the machine operates efficiently under both pump and turbine modes is a critical issue to solve. Thus, it is essential to investigate the hydraulic loss mechanism in two modes and improve the low specific speed pump-turbine design technology.

For the hydraulic loss in the low specific centrifugal pump, undesirable flows, such as separation, wake, and shock, are the main reason for the loss in the impeller, while the strong wall effect and incidence at the tongue are the dominant factors in the volute.[6] Li *et al.*[7] conducted a numerical simulation on the vortex movement of a pump-turbine in pump mode and found that the Dean vortex in the draft tube could cause periodic blockages in the stator passages and form the shock loss. When the pump runs in turbine mode, Tang *et al.*[8] concluded that the wall shear stress on the blade of the guide vane and runner, and the asymmetric vortex rope in the volute are the primary factors of irreversible energy loss. Ghorani *et al.*[9] indicated that the dominant dissipation occurs in PAT runner due to the shock at the blade inlet, flow deviation at the blade outlet, and vortices in flow passages. Cavazzini *et al.*[10] analyzed the unsteady behavior of the pump-turbine in pump mode and turbine mode. It is found that the rotating stall and the rotor–stator interaction are the leading causes for unstable operating in pump mode, which also amplifies the hydraulic loss, while the blocking effect of vortices and stall cells is responsible for the unstable phenomena in turbine mode. In addition, they also pointed out that many modifications on runner structures for improving turbine performance could negatively affect operation in pump mode, and it is essential to consider two modes simultaneously to optimize the structures.

Although almost all the studies mentioned the relationship between the vortex and hydraulic loss, the vortex identified by streamlines is limited to showing detailed flow information, as the streamlines

is a global method requiring values in many grid cells, which could ignore the local vortex structures presented by the neighborhood of a grid cell. There are many local vortex identification methods, such as vorticity, Q criterion,[11] and the λ_2 method,[12] but these methods are regarded as not precise enough to present the rotation motion of the fluid.[13] Based on the real eigenvector's direction of the velocity gradient tensor is the rotation axis of the local vortex and the rotation are supposed to avoid shear contamination. Liu *et al.*[14–16] proposed the rigid vorticity vector (also named as Liutex) to depict the rigid rotation of the fluid parcel, and a vorticity binary decomposition[17] was further presented to evaluate the local shear and rigid rotational strength. Since this method has been validated in many studies,[18–20] it could provide a special perspective to analyze the relationship between irreversible loss and local vortex strength.

Despite the above research, we also have conducted a series of studies on the detailed vortex flow features and induced loss in the pump, including entropy production diagnostic analysis,[21,22] structure optimization via minimization of entropy generation,[23] attached vortex patterns on the volute,[24] and unsteady rigid vortex evolution characteristics.[25] It is found that the entropy production method is an effective way to detect the detrimental flow and help to improve performance. However, the relationship between the vortices and loss is not fully understood, which leads to a lack of guidance in optimizing structures via vortex control. As improving the pump-turbine efficiency requires taking the flow analysis of both modes into account, the loss mechanism in the view of the local vortex in each mode needs to be further discussed.

In this paper, numerical research is conducted to investigate the flow characteristics in a low specific speed pump-turbine. The internal loss calculated by the entropy production method is validated in two modes. The relationship between loss and the local rigid vortex is revealed, and the flow and dissipation characteristics in both modes are discussed. Finally, an original hydraulic loss reduction method is validated in both modes based on the above findings.

II. THEORETICAL MODEL

A. Energy loss in pump-turbine

The total loss (TL) in the pump-turbine includes leakage loss, disk friction loss, and hydraulic loss. Although only the hydraulic loss is the research focus, the other two losses cannot be ignored when comparing the predicted performance with the experiment. The fluid could flow into the cavity chamber through clearance, which means this part of the fluid avoids any energy conversion by the runner. There exists leakage loss

$$\Delta P_L = \rho g q H, \tag{1}$$

where ρ is the density, q is the leakage flow discharge obtained from simulation, and H is the head.

Disk friction loss is related to the wall shear on the runner

$$\Delta P_D = \boldsymbol{\tau}_w \cdot \boldsymbol{u}_w, \tag{2}$$

where $\boldsymbol{\tau}_w$ is the wall shear stress, and $\boldsymbol{u}_w$ is the velocity at the first layer of the grid from the wall.

The hydraulic loss can be calculated by entropy generation based on the second law of thermodynamics. The single-phase instantaneous local entropy production with the Navier–Stokes equation form[26] is expressed as

$$S_{pro}^{NS} = \frac{\Phi}{T} - \frac{K}{T^2}\left(\frac{\partial T}{\partial x_i}\right)^2, \tag{3}$$

where Φ is the viscous dissipation, T is the temperature, K is the thermal conductivity, and x_i is the spatial coordinate. The first term of the right hand is loss from viscous dissipation, and the second term denotes irreversible heat transfer loss.

Since the heat transfer loss for the pump-turbine flow, which can be neglected due to the water temperature, is almost unchanged, the loss is dominated by viscous dissipation

$$\Phi = \sigma_{ij}\frac{\partial u_j}{\partial x_i}, \tag{4}$$

where σ_{ij} is the viscous stress, u_j is the velocity component. For the incompressible flow, $\sigma_{ij} = \mu(\frac{\partial u_i}{\partial x_j} + \frac{\partial u_j}{\partial x_i})$, and μ is the dynamic viscosity.

The instantaneous dissipation cannot be calculated directly except for direct numerical simulation data. Based on the idea of the Reynolds averaging method, the instantaneous viscous dissipation can be divided into time-averaged value and fluctuating component

$$\Phi_t = \bar{\Phi} + \Phi_t', \tag{5}$$

where $\bar{\Phi}$ is the time-averaged value, and Φ_t' is the fluctuating value.

Herwig and Kock[27] derived the entropy production equation with the Reynolds-averaged Navier–Stokes (RANS) form

$$\bar{\Phi} = \bar{\Phi}_d + \bar{\Phi}_{tur} = \mu\left(\frac{\partial \bar{u}_i}{\partial x_j} + \frac{\partial \bar{u}_j}{\partial x_i}\right)\frac{\partial \bar{u}_j}{\partial x_i} + \overline{\mu\left(\frac{\partial u_i'}{\partial x_j} + \frac{\partial u_j'}{\partial x_i}\right)\frac{\partial u_j'}{\partial x_i}}. \tag{6}$$

The first term of right hand is called direct dissipation, and the second is turbulent dissipation. Note that the turbulent dissipation is the average of fluctuation. The quantity is related to the turbulent dissipation rate

$$\bar{\Phi}_{tur} = \rho\varepsilon, \tag{7}$$

where ε is the turbulent dissipation rate.

Considering the turbulent production is generally approximately equal to the dissipation in a steady and homogeneous flow, the turbulent dissipation can also be expressed as[28]

$$\bar{\Phi}_{tur} = -\rho\overline{u_i'u_j'}\frac{\partial \bar{u}_i}{\partial x_j} = \mu_t\left(\frac{\partial \bar{u}_i}{\partial x_j} + \frac{\partial \bar{u}_j}{\partial x_i}\right)\frac{\partial \bar{u}_j}{\partial x_i}, \tag{8}$$

where the term $-\rho\overline{u_i'u_j'}\frac{\partial \bar{u}_i}{\partial x_i}$ is the turbulent production, $-\rho\overline{u_i'u_j'} = \mu_t(\frac{\partial \bar{u}_i}{\partial x_j} + \frac{\partial \bar{u}_j}{\partial x_i})$ is 'the Boussinesq's hypothesis, and μ_t is the turbulent viscosity.

The difference in turbulent dissipation between these two methods is slight, and the deviation is no more than 2%.[29] Thus, both of them can be used in the engineering field. The entropy production rate with RANS is expressed in Eq. (9), and Eq. (10) is the total hydraulic loss given as

$$S_{pro} = \frac{\bar{\Phi}_d}{T} + \frac{\bar{\Phi}_{tur}}{T}, \tag{9}$$

$$\Delta P_H = \int_V TS_{pro}dV. \tag{10}$$

This expression still works when it comes to unsteady Reynolds-averaged Navier-Stokes (URANS) or delayed detached eddy simulation (DDES) model, and Eq. (5) is recommended. During the transient process, the local entropy production can be obtained based on the instantaneous velocity and the turbulent dissipation rate.[30]

B. Vorticity binary decomposition

The necessary and sufficient condition of the fluid rotation requires that there exist two complex conjugates eigenvalues and a real eigenvector of the velocity gradient tensor, and the local rotational axis direct along the real eigenvector. Since the rotational axis of vorticity is not always satisfied with the condition, the curl of the velocity field can hardly present the physical phenomenon of rotation, i.e., vorticity concentrates in the Blasius boundary layer, but there does not exist fluid rotation. Liu *et al.* proposed the rigid vorticity vector $\boldsymbol{R}$ to represent the direction of the vortex and absolute swirling strength[17]

$$\boldsymbol{R} = R\boldsymbol{r} = \left[\boldsymbol{\omega}\cdot\boldsymbol{r} - \sqrt{(\boldsymbol{\omega}\cdot\boldsymbol{r})^2 - 4\lambda_{ci}^2}\right]\boldsymbol{r}, \tag{11}$$

where $\boldsymbol{\omega}$ is the vorticity, and $\boldsymbol{r}$ and λ_{ci} are the real eigenvector and the imaginary part of the complex eigenvalue of the velocity gradient tensor, respectively.

The rigid vorticity can be interpreted as the rigid-body rotation part of vorticity, and the other part of vorticity is mainly shear $\boldsymbol{S}$. Thus, the vorticity binary decomposition is expressed as

$$\boldsymbol{\omega} = \boldsymbol{R} + \boldsymbol{S}. \tag{12}$$

The local vortex exists when the magnitude of $\boldsymbol{R}$ is larger than 0. A non-dimensional variable Ω_R is also used in Eq. (13), which denotes the relative vortex strength.[31] As Ω_R becomes meaningful only when it is greater than 0.5, the Ω_{RB} in Eq. (14) is employed to represent the rotation directly[32]

$$\Omega_R = \frac{(\boldsymbol{\omega}\cdot\boldsymbol{r})^2}{2\left[(\boldsymbol{\omega}\cdot\boldsymbol{r})^2 - 2\lambda_{ci}^2 + 2\lambda_{cr}^2 + \lambda_r^2\right] + \varepsilon_0}, \tag{13}$$

$$\Omega_{RB} = \frac{|\Omega_R - 0.5| + (\Omega_R + 0.5)}{|2\Omega_R + 1| + \varepsilon_0}\Omega_R, \tag{14}$$

where λ_{cr} and λ_r denote the real part of the complex eigenvalue and the real eigenvalue of the velocity gradient tensor, respectively, and ε_0 is a small value to avoid program error.

III. NUMERICAL MODEL AND METHOD

A. Calculation domain

The centrifugal pump as turbine with a specific speed of $3.65nQ^{0.5}/H^{0.75} = 23.7$ was selected to conduct a numerical simulation in both pump and turbine modes. The designed head of the pump is 78 m under the discharge of 12.5 m^3/h and speed of 2900 r/min. Figure 1 shows the pump-turbine computational domain. Since only the fluid domain was modeled and simulated, the blank area in Fig. 1(c) presents the solid domain of the shaft and blades. Chambers A and B are the cavities to take the leakage loss into account. The red lines S1–S6 and light blue points V0–V4 denote the monitoring surface of the volute and the point, respectively. The surfaces S1–S4 are the cross sections of the volute at the degree of 90°, 180°, 270°, and 0°, respectively. The points V1–V4 locate in the corresponding position of circle C3 with a diameter of D_3. The S5 and V0 are aligned with the tongue tip. There are five flow passages in the runner, namely, P1–P5, as well as five parts for the curve C3. The main parameters of the fluid domain are listed in Table I. The length of the inlet tube and the outlet tube in pump mode is six and five times the diameter to reduce the disturbance, respectively. The structured mesh shown in Fig. 2 was built via ANSYS ICEM to improve the calculation efficiency, where the boundary layer grids near the blade suction side (SS) and pressure side (PS) are also illustrated.

B. Numerical setup

The ANSYS Fluent was applied for the transient flow calculation of the pump-turbine in two modes. The DDES based on the k–ω shear-stress transport (SST) turbulence model was selected to balance the calculation cost and precision.

In order to analyze the flow characteristic at the best efficiency point with the same rotational speed of two modes, the discharge rate of 6.25 m^3/h (Q_n) in pump mode and the discharge of 10.62 m^3/h ($1.7Q_n$) in turbine mode with the runner speed magnitude of 1450 r/min are defined. This runner speed is selected to avoid the plexiglass blades getting fragile during the experiment. The velocity inlet boundary and pressure outlet were set in pump mode, and the same boundary condition with a counter runner rotation was defined in turbine mode. The unsteady simulation of a moving mesh is employed when the initial steady calculation converges. The SIMPLEC scheme was chosen for pressure–velocity coupling. The time step is 0.000 115 s with 40 inner iterations, and the convergence criterion is 0.0001. The user-defined function was implemented to calculate the transient entropy production, rigid vorticity, and Ω_R in every time step.

C. Simulation validation

The grid convergence index (GCI) method recommended by the *Journal of Fluids Engineering*[33] was applied to validate the grid independence, and Table II gives the computed errors based on the Richardson extrapolation of three sets of grids in pump mode. As the fine-grid convergence index is less than 1%, the calculation result can be deemed to meet the demand for mesh independence. Thus, the pump-turbine model with 8.21×10^6 elements was selected in this paper. Under this set, the first grid layer heights near blades and volute are 0.003 and 0.016 mm, and the number of boundary layers is 16 and 10 with a growth ratio of 1.3, respectively. The average y+ of the runner blades is 1.8 and 5.4 of the volute wall.

The experiment was conducted to validate the numerical method, where the uncertainty of head and efficiency are 0.4% and 0.66%, respectively, according to the measurement uncertainty and calculation formula. The detailed information on the hydraulic test loop can be seen in our previous paper.[24] Figure 3(a) presents the changes in head and efficiency with different discharges in pump mode, where the pump head and efficiency are expressed as Eqs. (14) and (16). In general, the predicted results agree well with the experimental data, and the maximum error is lower than 3%, which indicates the simulation is reliable. The comparison of the entropy production method is shown in Fig. 3(b), where the total loss (TL) was calculated by Eqs. (18) and (19). The maximum total loss error in different methods is 5% in pump mode and error of 4% in turbine mode. Although only

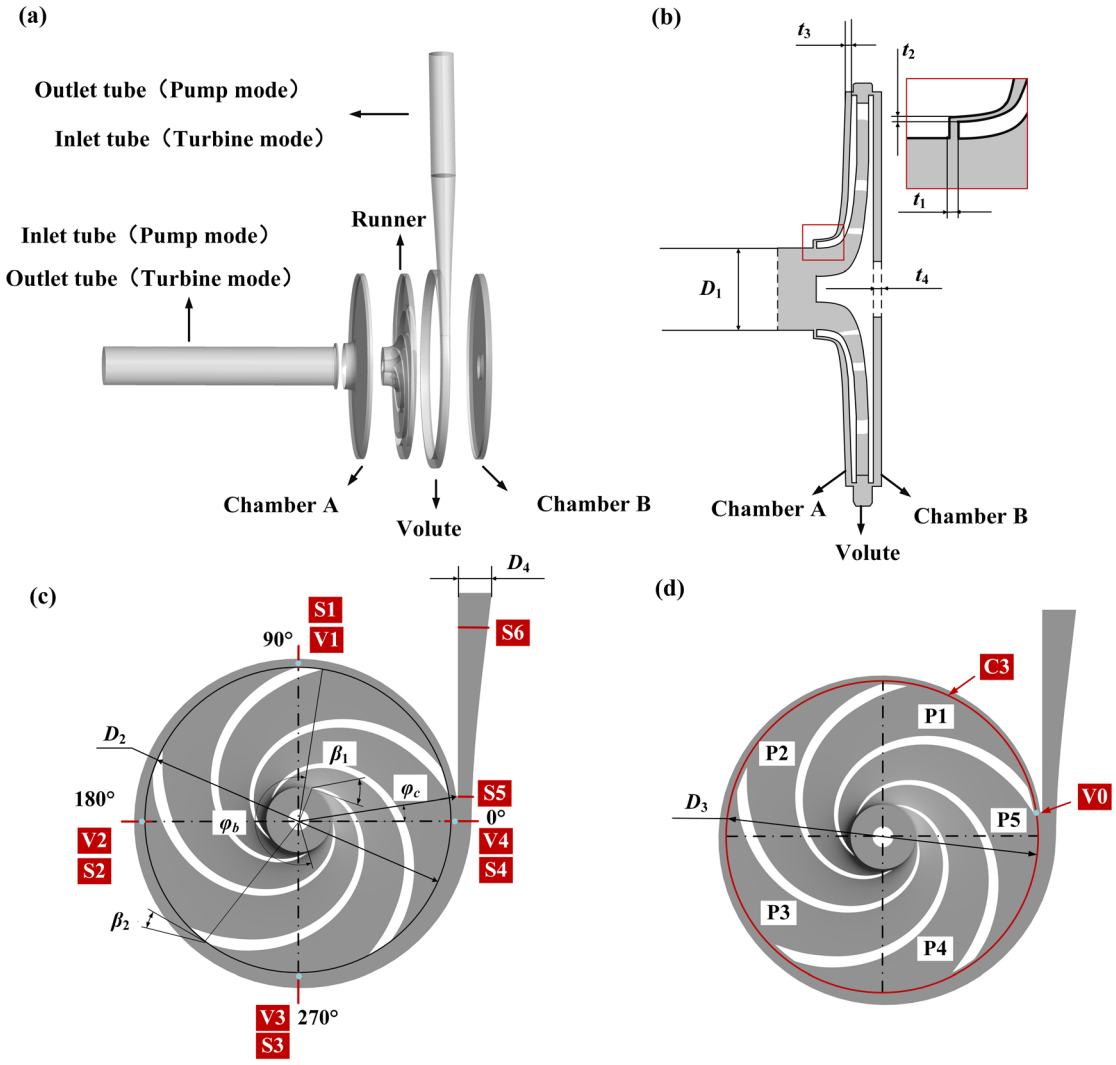

FIG. 1. The computational domain of the pump-turbine and schematic view: (a) components in two modes, (b) side view of the runner and the volute, (c) front view of the runner and the volute with monitor points, and (d) front view of the runner and the volute with monitor curve.

TABLE I. Geometric parameters of the pump-turbine.

Variable	Value	Variable	Value
D_1	0.05 m	D_2	0.236 m
D_3	0.242 m	D_4	0.0319 m
φ_b	230°	φ_c	9°
β_1	29°	β_2	19.1°
t_1	0.002 m	t_2	0.001 m
t_3	0.004 m	t_4	0.005 m

numerical data were used to validate the entropy production method in turbine mode, the total loss computed via the experimental data and numerical data given in pump mode is sufficient to verify the validity and accuracy of this method

$$H_P = \frac{p_{out} - p_{in}}{\rho g}, \tag{15}$$

$$H_T = \frac{p_{in} - p_{out}}{\rho g}, \tag{16}$$

$$\eta_P = \frac{\rho g Q_P H_P}{M_P \omega_r}, \tag{17}$$

$$\eta_T = \frac{M_T \omega_r}{\rho g Q_T H_T}, \tag{18}$$

$$\Delta P_{TL,P} = M_P \omega_r - \rho g Q_P H_P, \tag{19}$$

$$\Delta P_{TL,T} = \rho g Q_T H_T - M_T \omega_r, \tag{20}$$

where the subscripts P and T denote the pump mode and the turbine mode, respectively, H is the head, η is the efficiency, p_{out} and p_{in} are

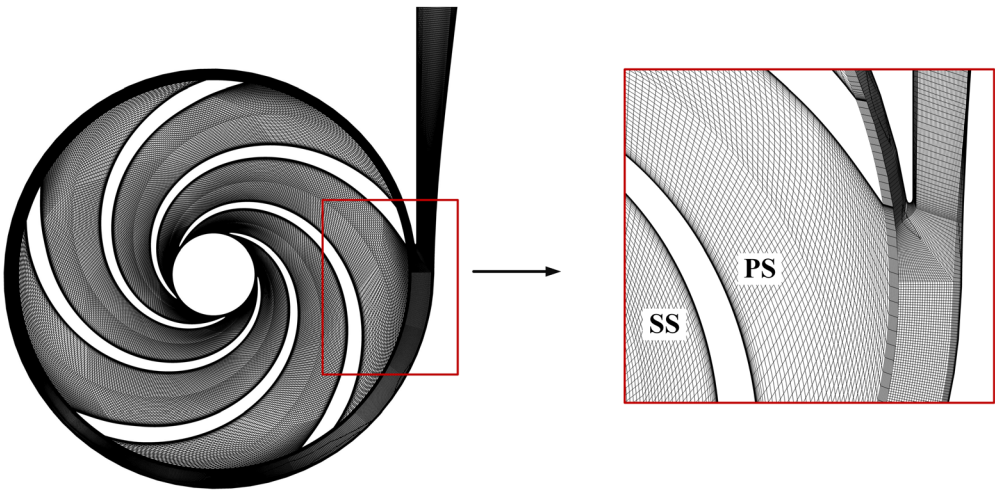

FIG. 2. Grid information of the runner and the volute.

TABLE II. Grid convergence index based on the Richardson extrapolation method.

Parameters	Variable	Value
Mesh element number	M_1, M_2, M_3 ($\times 10^6$)	3.64, 5.47, 8.21
Grid refinement factor	r_{21}, r_{32}	1.5, 1.5
Head	H_1, H_2, H_3 (m)	19.42, 19.33, 19.28
Apparent order	P	1.44
Extrapolated value	$\Phi^{21}{}_{\text{ext}}$	19.53
Approximate relative error	$e^{21}{}_{\text{a}}$ (%)	0.46
Extrapolated relative error	$e^{21}{}_{\text{ext}}$ (%)	0.58
Fine-grid convergence index	$\text{GCI}^{21}{}_{\text{fine}}$ (%)	0.72

the total pressure at the outlet and the inlet, M is the torque, Q is the flow discharge, and ω_r is the angular velocity.

IV. RESULTS AND DISCUSSION

A. Loss characteristic of local rigid vortex in pump mode

This part focuses on the relationship between hydraulic loss and local vortex, and their characteristics under typical unsteady flow phenomena, such as jet-wake flow and the rotor–stator interaction in pump mode.

The instantaneous contour of the entropy production rate and local rigid vortex distribution with streamlines at the mid-plane of the runner and the volute at discharge of Q_n are shown in Fig. 4.

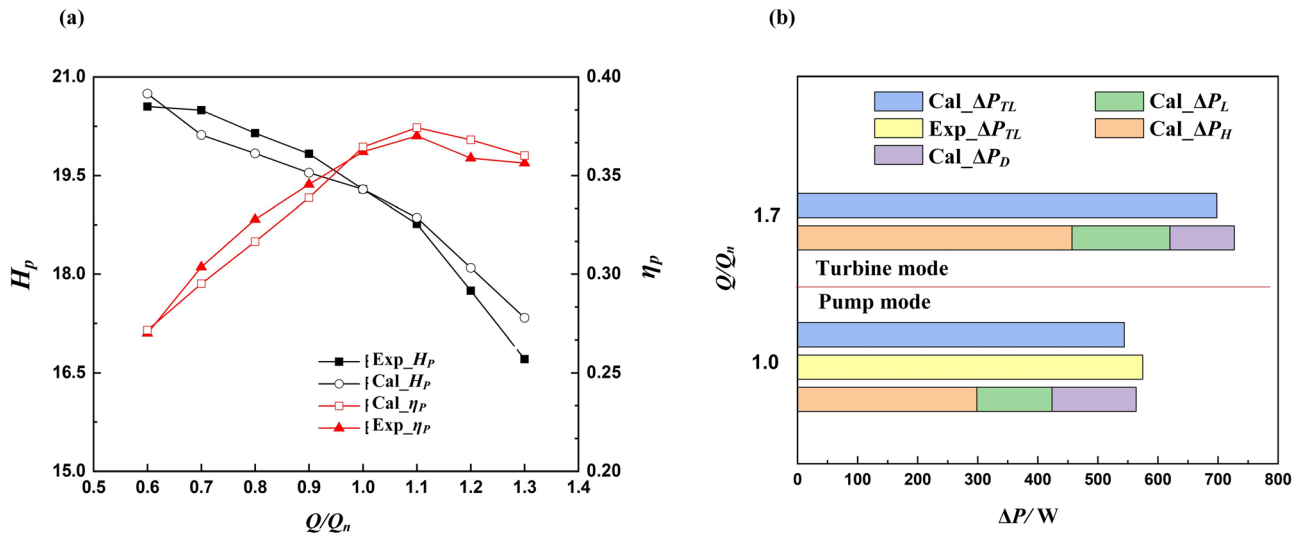

FIG. 3. Performance comparison between experimental and numerical results: (a) validation on head and efficiency in pump mode and (b) validation on the entropy production method.

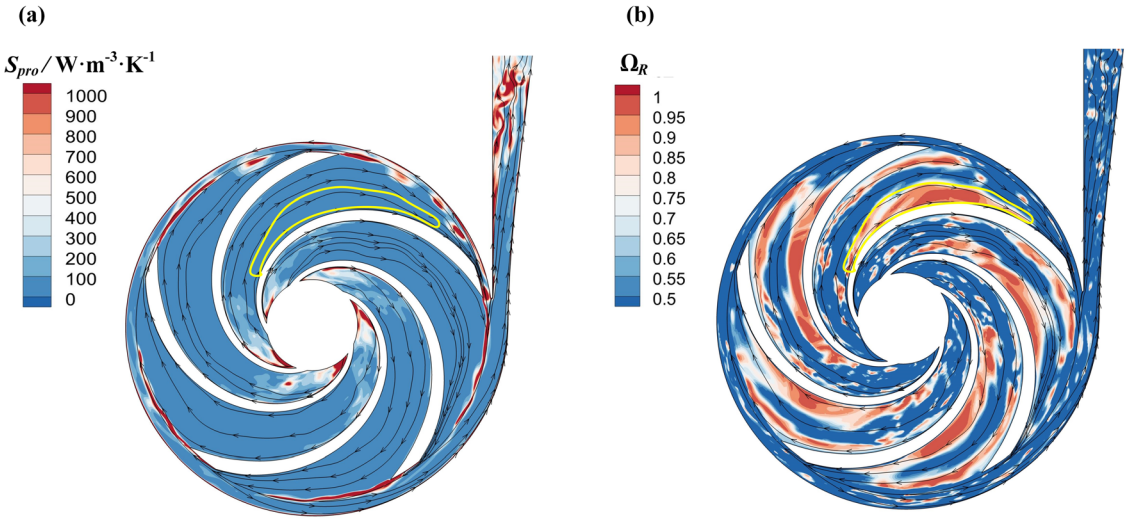

FIG. 4. Distribution of hydraulic loss and local rigid vortex in pump mode: (a) contour of entropy production rate and (b) contour of the relative vortex strength.

The loss concentrates on the runner inlet, runner outlet, and volute outlet. The incidence loss at the leading edge of blades accounts for the significant entropy production at the runner inlet, while the wake flow is the leading cause of loss at the runner outlet. In addition, there also exist high losses at the blade tip clearance when the blade moves to the volute tongue. Streamlines present the distribution of the global vortex, indicating a smooth flow in the runner without any separation and vortex on a mainstream scale. However, the local vortex identification method could illustrate more detailed vortex structures. Figure 4(b) shows the local rigid vortex structures. It can be seen that there are fewer vortices at the runner inlet while generating sharply in the runner passages near the suction side and pressure side. At the runner outlet, vortices concentrate on the wake flow of the trailing edge of the suction side, and there are no apparent vortices near the pressure side. Although some studies indicate that the vortex structures could lead to local loss rise,[9] there exists a counterexample that the vortices in the runner passages do not cause significant loss, as shown in the area marked by the yellow curve, where there exist intense vortex structures while the local loss is almost negligible.

The jet-wake flow pattern is a common phenomenon occurring at the outlet of the centrifugal runner, which is featured higher velocity near the pressure side of the blade (jet flow) and lower velocity near the suction side (wake flow), causing a considerable impact on efficiency. In Fig. 5, the instantaneous velocity and the entropy production rate on circle C3 were further extracted to analyze the loss distribution in jet-wake flow. Assuming the velocity of the turning point (the boundary between the jet and wake) was the spatially averaged value in each part of P1 to P5, the approximate areas of the jet

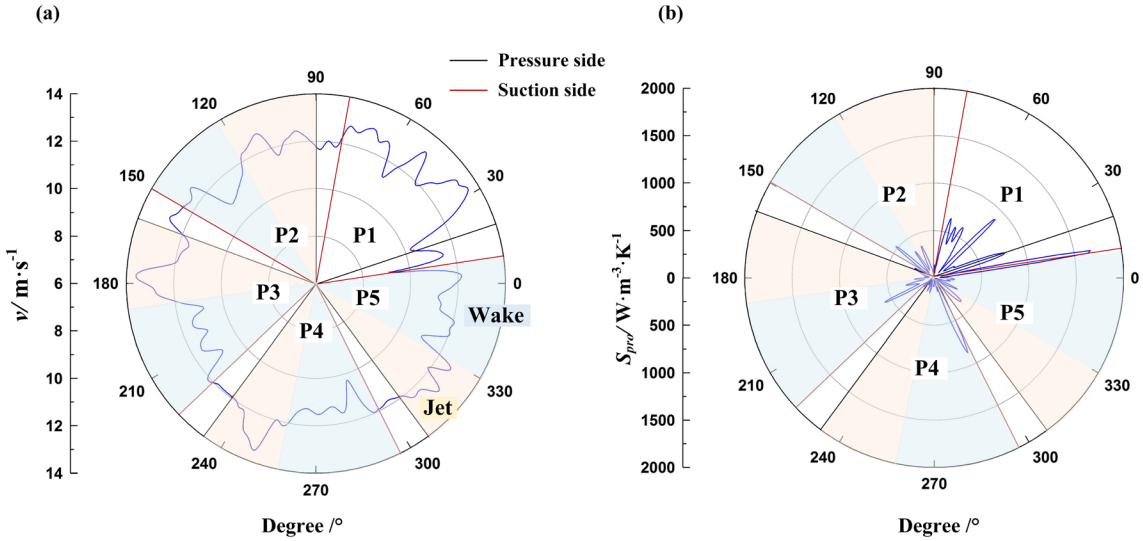

FIG. 5. Distribution of velocity and hydraulic loss at C3 in pump mode: (a) velocity and (b) entropy production rate.

pattern marked in light orange and the wake pattern in light blue in each passage were divided, except for the passage P1, as there is no apparent jet-wake pattern. Figure 5(b) also shows that hydraulic loss mainly occurs in the wake areas and achieves the highest level at the suction side in passage P5 when the blade moves to the tongue region.

Since vorticity binary decomposition provides the perspective of pure shear distribution and local rigid vortex strength, the relationship between loss, shear, and rotational strength can be further revealed. The top diagram of Fig. 6 depicts the shear and loss changes in the jet-wake pattern, and the bottom one gives the distribution of absolute vortex strength $\boldsymbol{R}$ and relative strength Ω_{RB}. The hydraulic loss is closely related to shear as the shear trend agrees well with the entropy production rate. Compared with the average entropy production rate of the wake areas and the jet regions, the average wake loss can be 1.6 times higher than the loss in jet flow. According to the distribution of shear and rotational strength, it is found that the shear is a necessary but insufficient condition to the local vortex, i.e., there could be no vortex occurring even if strong shear exists as shown in the jet area in P5. However, once a local rigid vortex exists, the absolute rotational strength could rise with the increasing shear. It is also noted that the hydraulic loss near point B is considerably lower than that near point A when the values of shear are almost identical. This can be explained by the difference in rotational strength that the magnitude of $\boldsymbol{R}$ at point B is much higher than that at point A. It can be concluded that the areas with higher rotational strength can be less dissipated than others when suffering a comparable shearing effect.

The instantaneous distribution of loss and vortex in the cross sections of the volute is present in Fig. 7, where the subscript number of T1–T4 and B1–B4 corresponds to the position S1–S4. In the top diagrams T1–T4, the loss from the two opposite pairs of global vortices is much less than the loss produced by wall shear, and it is also substantially lower than the incidence loss when the blade passes the tongue in T4. Thus, reducing the wall shear or incidence loss at the tongue can be more efficient than controlling secondary flow to decrease energy dissipation. The bottom figures B1–B4 show the relationship between local rigid vortices and the global vortex. The global vortex (vortex identified by the global method) is depicted by streamlines as this method requires values in many grid cells, while the local vortex (vortex identified by the local method) is presented by the neighborhood of a grid cell. The global method hardly captures all the local vortex's positions, but the local vortex could present all the central positions of the global vortex. The possible reason is that the global vortex featured plenty of local vortices rotating around a public axis. So, it can be concluded that the generation of the local vortex is a necessary but not an insufficient condition for the global vortex. In addition, the local rigid rotational strength has little connection with the central location of the secondary flow.

The rotor–stator interaction is another critical factor for pump operation in a stable and high-efficiency state. It is known that this effect could amplify hydraulic loss, while the amplitude of loss differs from region to region in the volute because of the asymmetric structure and the influence of the volute tongue. To analyze how the loss in different regions is affected by the rotor–stator interaction and where is the most dissipated area, the fast Fourier transform (FFT) of the change of the entropy production rate at points V0–V4 was presented in Fig. 8. The 1024 sample points in three rotation periods were used to satisfy the requirement of the sample number (2^n) of FFT. This number of rotation periods can be sufficient to show the changing law and save the computation cost at the same time. The spectra domain diagram shows that the dominant frequency locates at blade passing frequency (f_{BPF}), where the peak loss decreases from point V0 to V4 along the downstream direction. Due to the tongue effect, the maximum loss at f_{BPF} at V0 can be approximately three times higher than the loss at V3. This is because the shearing effect gets reduced since

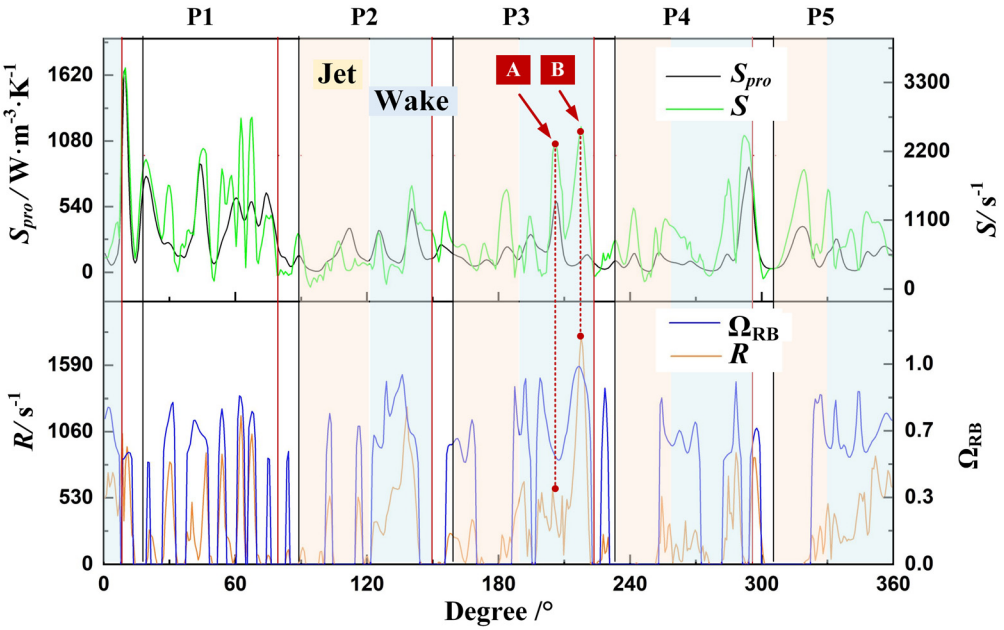

FIG. 6. Distribution of hydraulic loss, shear, and rigid vortex strength at C3 in pump mode.

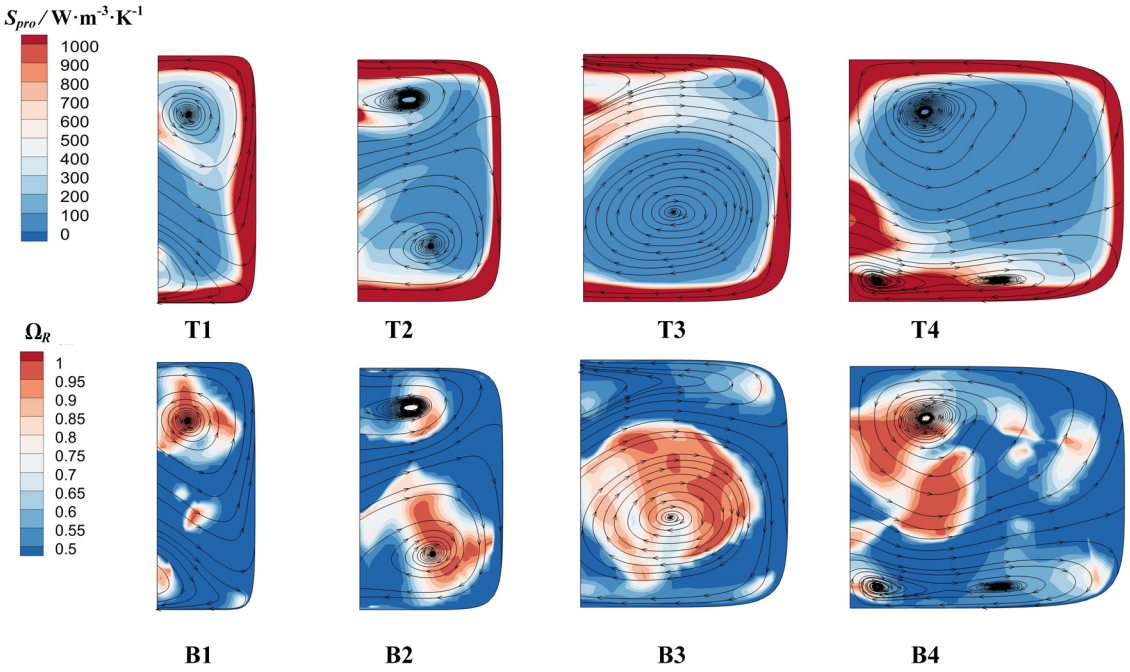

FIG. 7. Distribution of hydraulic loss and local rigid vortex in pump mode. T1–T4 are the contours of the entropy production rate at sections S1–S4, respectively, B1–B4 contours of the relative vortex strength at sections S1–S4, respectively.

the blade tip clearance becomes wide. Figure 9 shows the changes in shear, rigid vortex strength, and loss at point V0 during the rotor–stator interaction process. In the time domain graph, the start time is when the phase position of the runner equals it of Fig. 4. The changing trend of shear instead of rotational strength is consistent with hydraulic loss, which proves again that it is shear that plays a major role in energy dissipation. However, the relationship between shear and rotational strength can be complicated since the magnitude of shear is not the only factor in vortex generation. A periodic phenomenon can be seen that all these variables reach their highest level when the blade passes by the volute tongue. The spectra domain diagram shows the dominant frequency locates at the blade passing frequency, and distinct shear and hydraulic loss peaks occur at its harmonics. The amplitude of rigid vorticity pulsation is distinctive only at f_{BPF} and 2 f_{BPF}, indicating the high-frequency vortices are characterized by chaotic and weak vortices, while the loss and shear can be more sensitive to the rotor–stator interaction in a broader range of frequency.

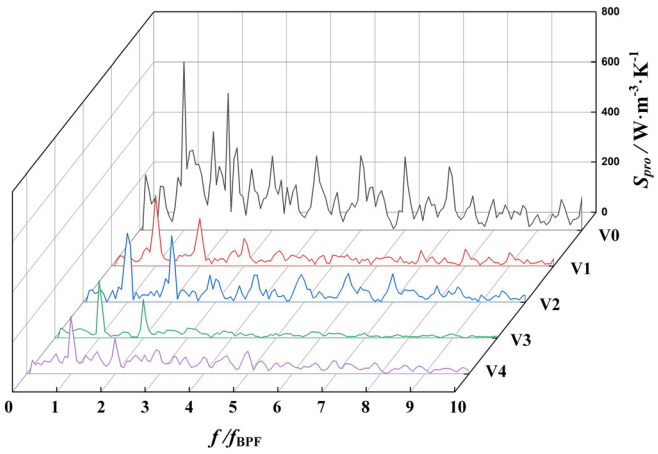

FIG. 8. FFT spectra of the entropy production rate at different monitor points in pump mode.

It is aware that hydraulic loss is not only dominated by shear but also negatively associated with rotational strength from the above discussion. However, the increase in the rotational strength always accompanies the strengthening of shear. Thus, the relative quantity of the ratio of shear to rigid vorticity (RSL) in Eq. (21) is proposed to quantify the influence of shear on the rigid rotational strength. When the value of RSL decrease, the flow tends to be steady with loss reduced since the relative rotational strength gets enhanced, and the shearing effect is likely to strengthen rotation rather than dissipate. Figure 10 shows the area averaged energy loss and RSL on the iso-surface of vortex structures identified by Ω_{R} under the instantaneous field. The areas are iso-surface of Ω_R at 0.5, 0.6, 0.7, 0.8, and 0.9. Once the coordinates of these points of iso-surface were extracted, the spatially averaged value of S_{pro} and RSL can also be obtained. The total loss in the volute is much higher than the loss in the runner. Both the loss and RSL of vortices become lower as relative rotational strength gets stronger, indicating that the RSL can be used as a subordinate factor in contrast with shear to hydraulic loss,

$$\mathrm{RSL} = \frac{|\boldsymbol{S}|}{|\boldsymbol{R}| + \varepsilon_0}. \tag{21}$$

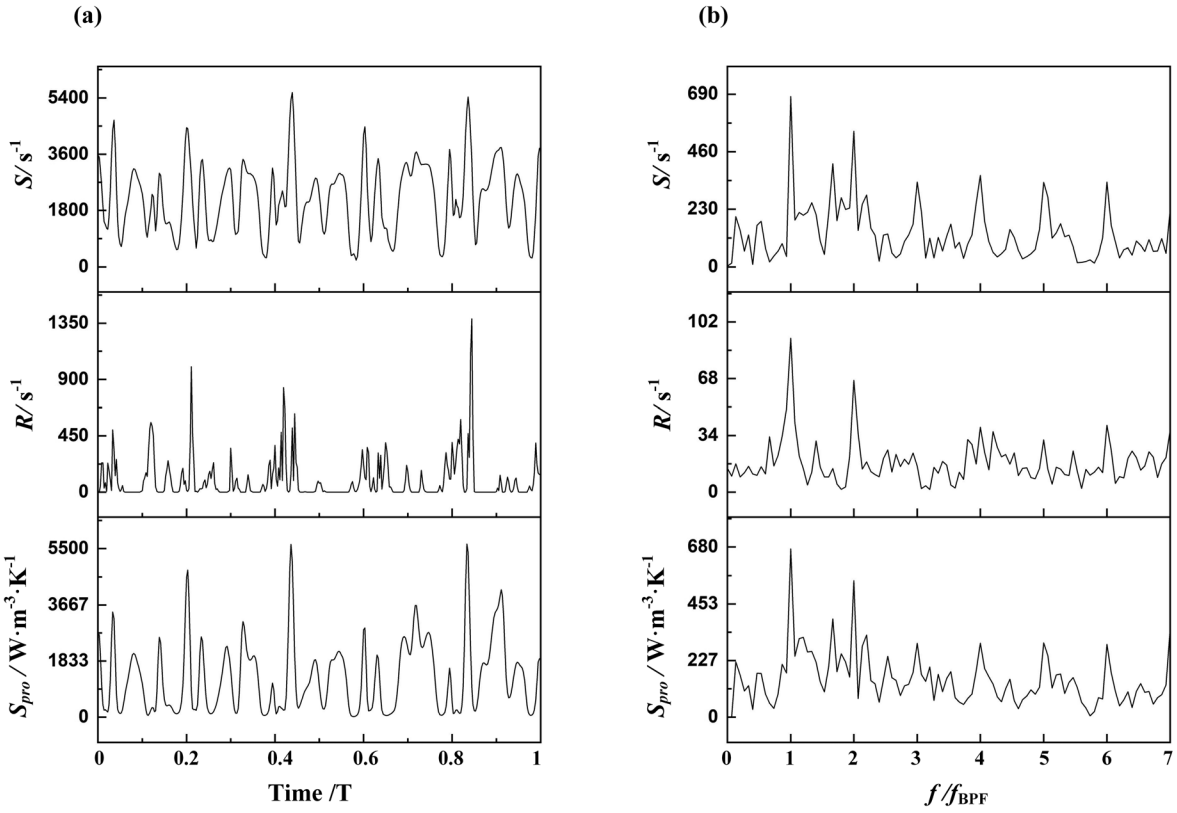

FIG. 9. Local vortex and loss characteristics of the rotor–stator interaction at monitor point V0 in pump mode: (a) temporal evolution of the shear, rigid vorticity, and entropy production rate and (b) FFT spectra of the shear, rigid vorticity, and entropy production rate.

B. Loss characteristic of local rigid vortex in turbine mode

This part focuses on the difference in loss distribution affected by the local rigid vortex and shear in turbine mode compared to pump mode under the turbine best efficiency point ($1.7Q_n$) with unchanged rotational speed. The representative flow patterns of separation, jet-wake flow, and rotor–stator interaction are also discussed.

The hydraulic loss mainly concentrates in spiral casing wall, runner blades tip, and runner inlet passages and also exists at the runner outlet in a small proportion according to Fig. 11. Although the global

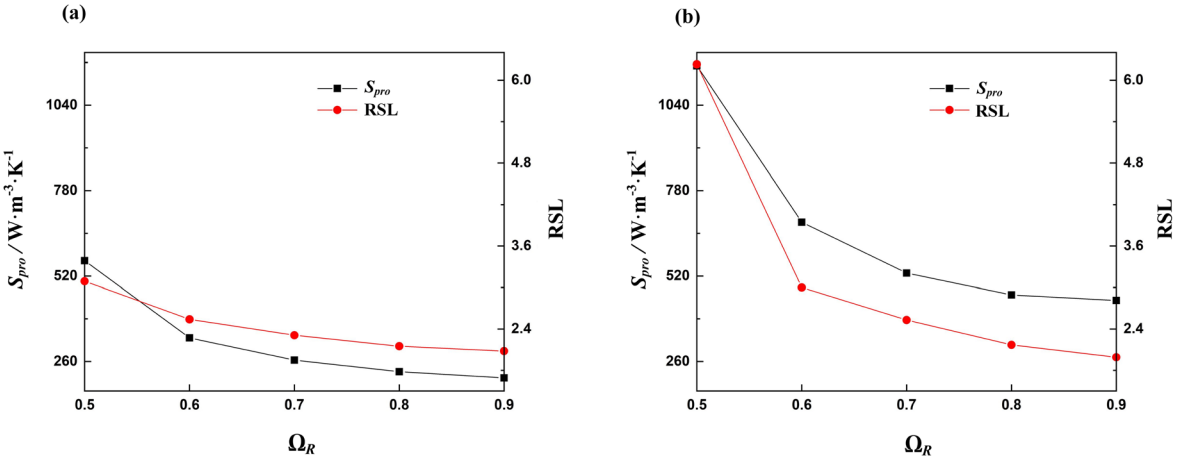

FIG. 10. Comparison between the area-averaged entropy production rate and RSL vs relative vortex strength in pump mode: (a) in the runner and (b) in the volute.

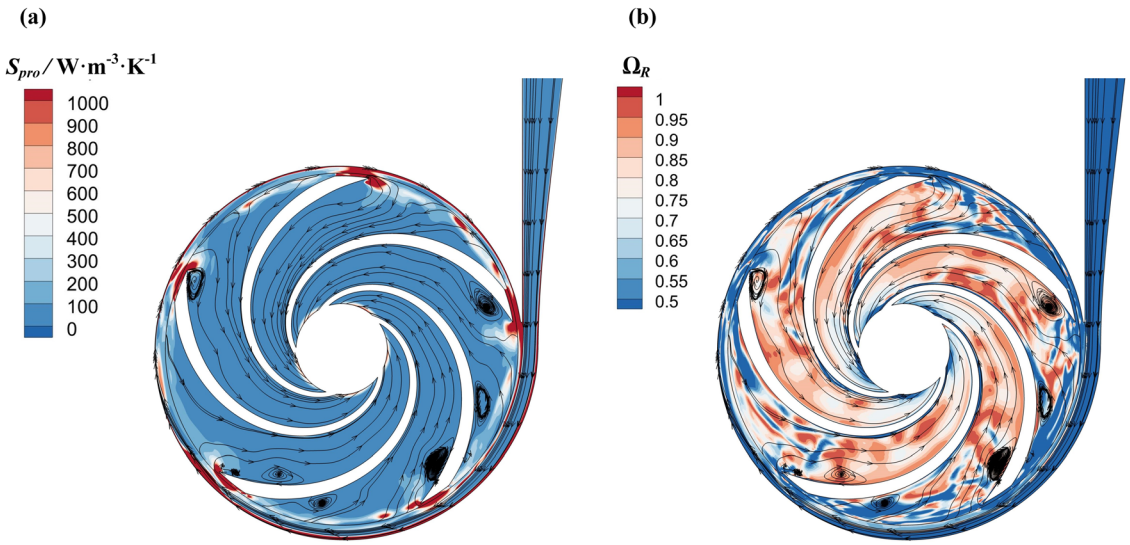

FIG. 11. Distribution of hydraulic loss and local rigid vortex in turbine mode: (a) contour of the entropy production rate and (b) contour of the relative vortex strength.

vortices of separation flows occur in the runner passages, it does not bring plenty of losses as flow in blades tip or near spiral casing wall. There are no obvious axial local rigid vortices in the volute except for the downstream spiral casing. The axial vortices almost cover the whole runner passages, while they are only found near blades in pump mode.

The flow pattern of velocity magnitude periodically varying from high to low value in passages is also found in turbine mode, as shown in Fig. 12(a), where the sampled points are identical to those in pump mode. Although it occurs in the runner inlet, it is also named the jet-wake phenomenon in this paper. However, in contrast to pump mode, the jet is near the suction side, and the wake is near the pressure side in turbine mode. In addition, there is no significant loss in the wake areas compared to the jet areas, as shown in Fig. 12(b), while the loss at the tip of the blade takes the majority proportion. The counter pattern of velocity distribution in two modes is attributed to the reversed flow condition and vortices distribution. In pump mode, the combination effect of adverse pressure gradient flow in the runner and the wake vortices causes the lower velocity magnitude in the wake areas. However, as the flow in turbine mode is favorable pressure gradient, the velocity magnitude near the suction side can be higher due to the higher-pressure gradient on the suction side compared to the pressure side.

In addition to the difference in wake loss between the two modes, the significant loss in the wake areas of pump flow appears due to intense shear, while in turbine mode, there is no considerable shear in the wake flow to promote loss generation, as depicted in Fig. 13. It is also found the phenomenon that the hydraulic loss decreases even

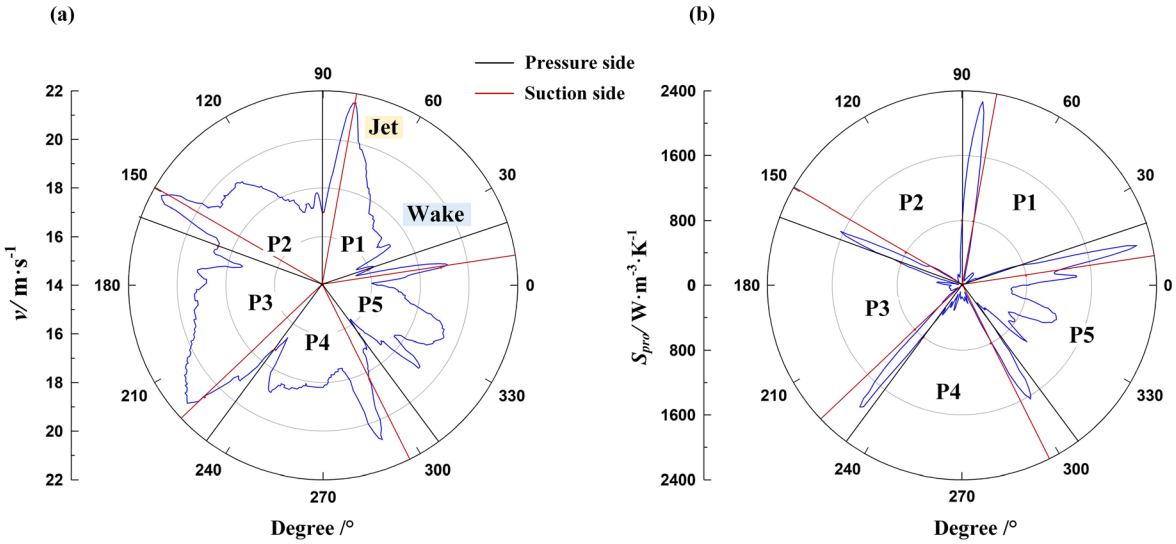

FIG. 12. Distribution of velocity and hydraulic loss at C3 in turbine mode: (a) velocity and (b) entropy production rate.

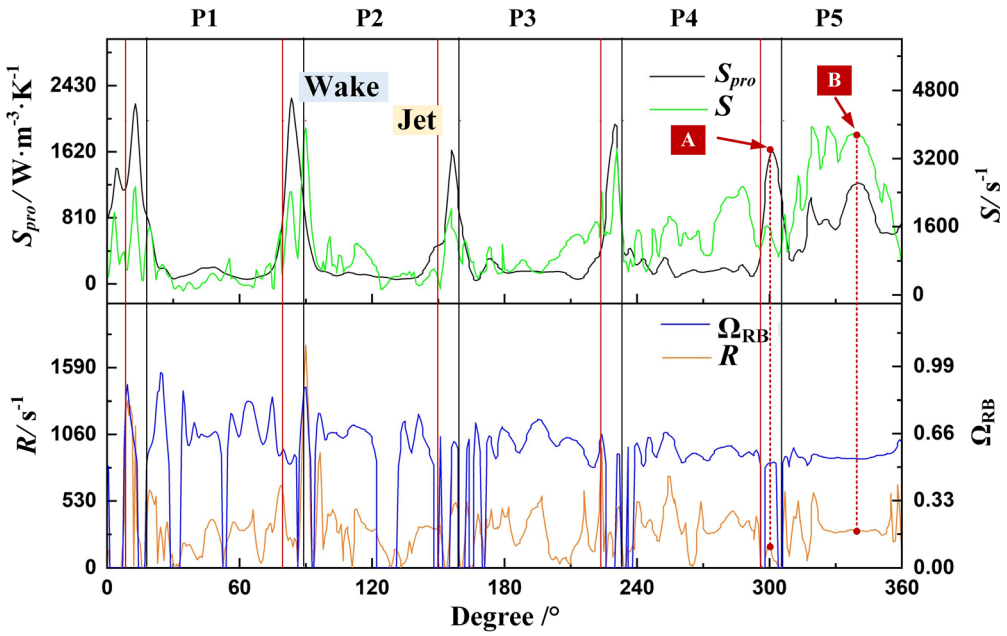

FIG. 13. Distribution of hydraulic loss, shear, and rigid vortex strength at C3 in turbine mode.

when shear increases at point B of P5. This is because the strength of the local rigid vortices is reinforced and make the local loss less dissipated, which verifies the previous conclusion.

The hydraulic loss and local vortices distribution of spiral casing is given in Fig. 14, where the subscript number of T1–T4 and B1–B4 also corresponds to the position S1–S4. The change of loss along the downstream in turbine mode is more significant compared to pump mode, and the area-averaged hydraulic loss reaches a maximum at the end of the monitor section shown in T1. In addition, no streamwise global vortex is observed in section T4, and only a few local vortices appear at the volute outlet. As discussed in pump mode, a pair of opposite vortices are also found with fluid flows downstream.

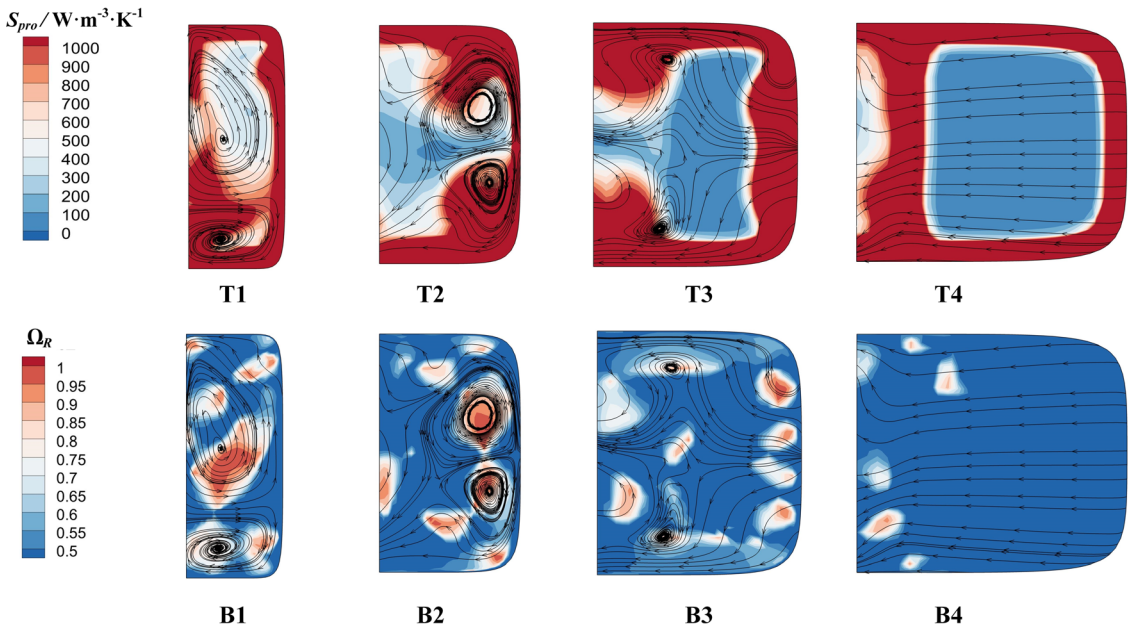

FIG. 14. Distribution of hydraulic loss and local rigid vortex in turbine mode. T1–T4 are the contours of the entropy production rate at sections S1–S4, respectively, B1–B4 are contours of the relative vortex strength at sections S1–S4, respectively.

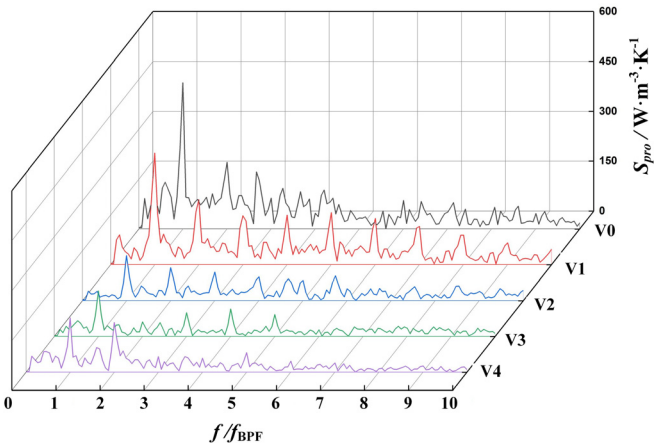

FIG. 15. FFT spectra of the entropy production rate at different monitor points in turbine mode.

Meanwhile, more and more local vortices are generated due to the intense unsteady flow downstream.

When the monitor point locates upstream of the runner in turbine mode, a similar rotor–stator interaction effect is also observed in Fig. 15 compared to pump mode. Although the local loss is higher than it is in pump mode, the amplitude of loss fluctuation is smaller. The loss caused by the rotor–stator interaction with a tongue effect can also be up to threefold over the loss without a tongue effect.

The changes in shear, rotational strength, and hydraulic loss near the volute tongue are shown in Fig. 16. The blade passing frequency is also the dominant frequency. The values of shear and loss are much smaller than those in pump mode even though the volute flow velocity in turbine mode is higher than in pump mode, indicating that the blade passing effect on dissipation in turbine mode is rather weaker compared to pump mode. However, unlike the vortex strength pulsation in pump mode, a distinct peak occurs at $2f_{RF}$, which implies there may exist a rotating stall causing local vortex generation periodically but with negligible impact on loss.

C. Hydraulic loss reduction based on passive control of shear and RSL

According to the above discussion, the local hydraulic loss could decrease when shear or RSL gets reduced, and the shearing effect plays a major role. It can be feasible to improve the efficiency of the pump-turbine in both modes by reducing shear or strengthening rigid vortex via structure optimization.

Since the loss near the volute outlet in pump mode and the incidence loss near the volute tongue in both modes are the significant factors to the whole hydraulic loss, the adjustment of the volute tongue

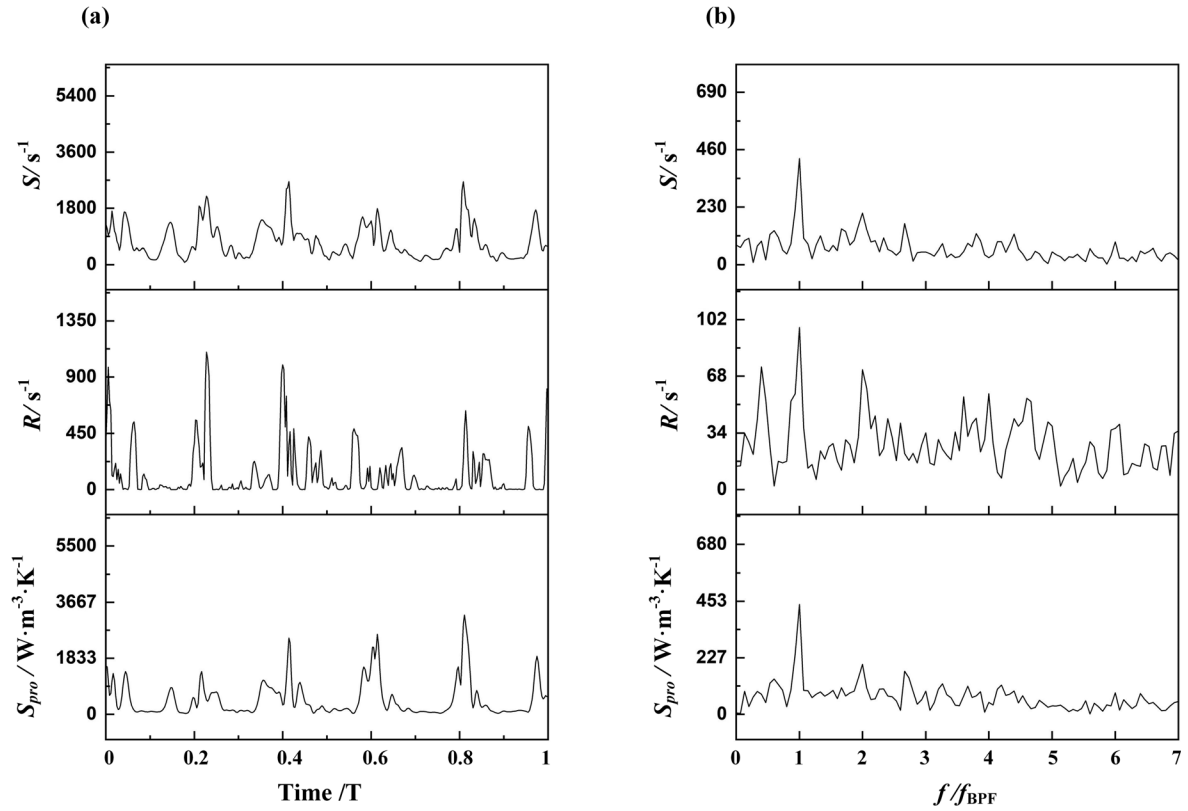

FIG. 16. Local vortex and loss characteristics of the rotor–stator interaction at monitor point V0 in turbine mode: (a) temporal evolution of the shear, rigid vorticity, and entropy production rate and (b) FFT spectra of the shear, rigid vorticity, and entropy production rate.

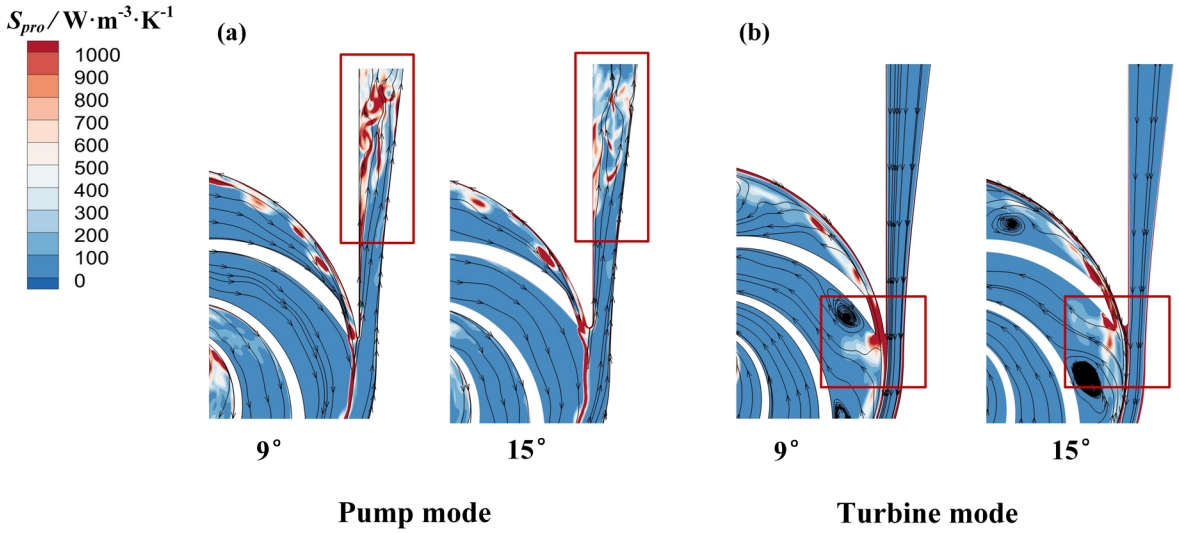

FIG. 17. Comparison of hydraulic loss and local vortices for pump-turbine in two modes: (a) pump mode and (b) turbine mode.

angle from 9° (original pump-turbine) to 15° (optimized pump-turbine) was applied to reduce energy loss. It should be pointed out that the thought of current modification was enlightened by an experiment study.[34] Although it may not be effective in other models, the basic idea of shear and relative rigid rotational strength control is the critical issue.

When the tongue angle increases, the hydraulic loss in the downstream region of the volute in pump mode and the loss near the tongue

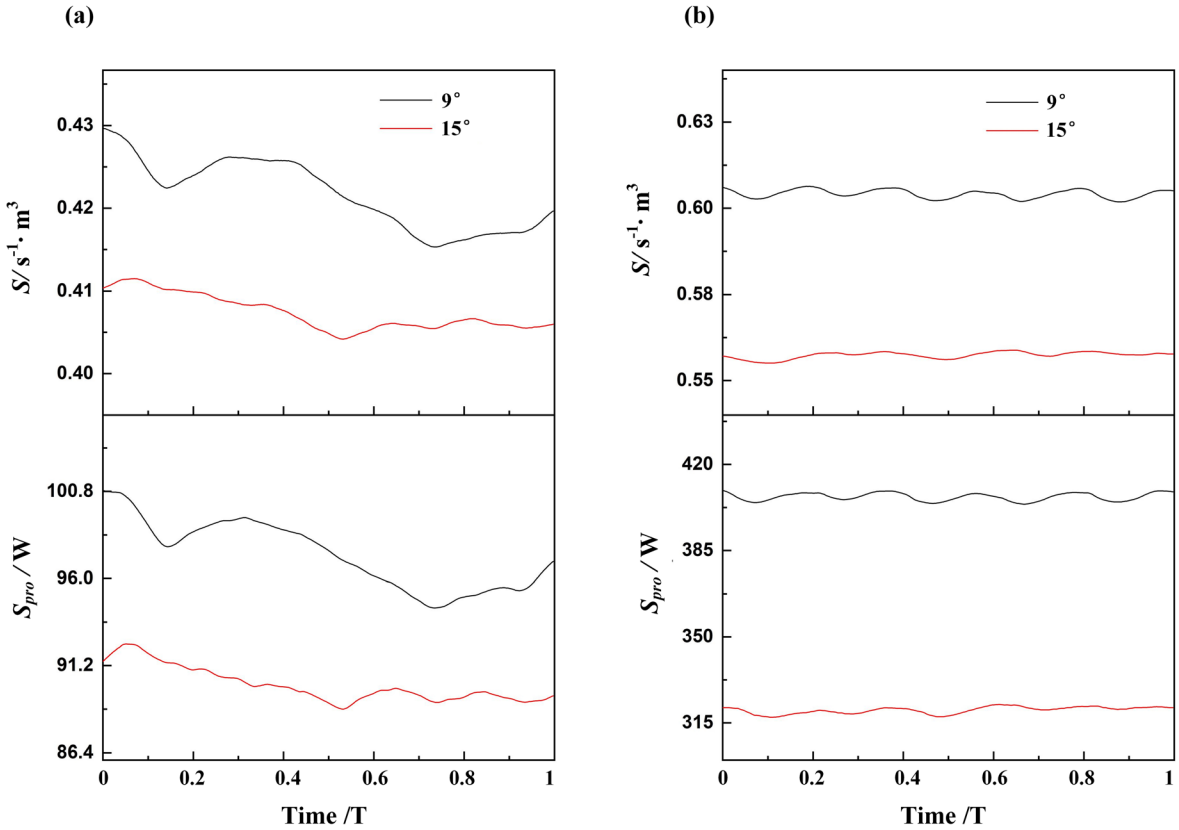

FIG. 18. The temporal evolutions of volume integral hydraulic loss and shear in the volute: (a) in pump mode and (b) in turbine mode.

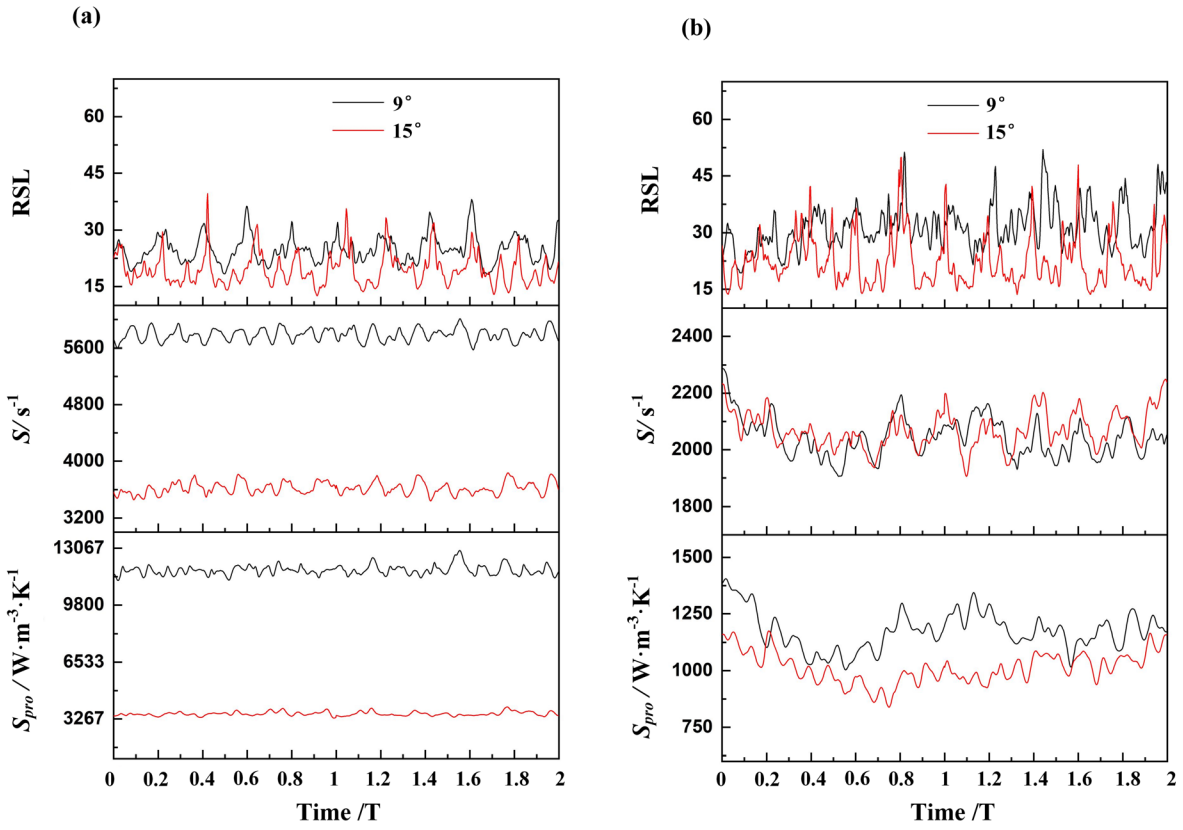

FIG. 19. The temporal evolutions of area-averaged hydraulic loss, shear, and RSL in pump mode: (a) at surface S5 and (b) at surface S6.

in turbine mode, as marked with the red rectangle in Figs. 17(a) and 17(b), gets reduced compared to the original pump-turbine. Figure 18 gives the change of total hydraulic loss and shear in the volute within a rotational period, which shows there is less loss in optimized volute all the time. In addition, the loss in turbine mode featured periodic fluctuation, while it is not observed in pump mode. This phenomenon implies that the effect of the rotor–stator interaction on volute loss in turbine mode is the main factor, while this effect is not dominant in pump mode when compared to the loss downstream of the volute tongue.

In order to analyze the detailed variation in shear and relative rigid rotational strength in the downstream volute regions in pump mode, the area-averaged values at cross sections S5 and S6 were monitored, as shown in Fig. 19. Note that the position of S5 is aligned with each tongue tip, and S6 locates the same place in two models. At the tongue tip area S5, the average loss of the optimized pump is less than that of the original pump over the periods due to the shear decrease after optimization. However, when the average shear at S6 in the optimized one becomes almost identical, the RSL could help explain the reduction in loss. Due to the smaller value of RSL, the flow tends to be less dissipated as the relative rotational strength becomes reinforced. Thus, the local shear and RSL are not only helpful in explaining the hydraulic loss generation but also are practical objectives for structure optimization.

V. CONCLUSIONS

By applying the DDES simulation with the help of the entropy production method and vorticity binary decomposition, this study analyzed the influence of local shear and rigid rotational strength on hydraulic loss in a low specific speed pump-turbine, and their distribution characteristics of typical unsteady flow phenomena in both modes. An original idea of reducing local hydraulic loss is also discussed based on the findings. The main conclusions are drawn as follows:

(1) Local shear is the main factor to hydraulic loss rather than the occurrence of local vortices or global vortices, such as secondary flow and separation flow, since the occurrence of these vortices does not always imply intense shear. In addition, vortex areas with lower RSL can be less dissipated in comparison to others under the comparable shearing effect.
(2) In contrast to the jet-wake flow in pump mode, this pattern in turbine mode is characterized by higher velocity near the suction side and lower velocity near the pressure side due to the significant favorable pressure gradient on the suction side. There is little difference in the distribution of shear and vortices in the wake flow in turbine mode, while the average wake loss can be 1.6 times higher than the loss in the jet regions in pump mode.

(3) The local loss caused by the rotor–stator interaction with a tongue effect at blade passing frequency can be up to three times higher than the loss without a tongue effect in both modes. However, this impact on the hydraulic loss of the volute in turbine mode is weaker than in pump mode. Nevertheless, the blade passing effect plays a more vital role in the volute loss in turbine mode, as periodic loss fluctuation in the volute is observed in turbine mode rather than pump mode.
(4) Reducing local shear and RSL of the local vortices is an effective way to decrease local hydraulic loss. The pump-turbine performance can be improved by optimizing the volute tongue angle to reduce loss via decreasing the local shear at the tongue area in both modes and lowering RSL of local vortices downstream of the volute in pump mode.

ACKNOWLEDGMENTS

This work was supported by the National Natural Science Foundation of China (Grant Nos. 51876220 and 52179094) and the China Scholarship Council (Grant No. 202006440097).

AUTHOR DECLARATIONS

Conflict of Interest

The authors have no conflicts to disclose.

Author Contributions

Zhiyi Yuan: Conceptualization (lead); Formal analysis (lead); Investigation (lead); Methodology (lead); Validation (lead); Writing – original draft (lead); Writing – review & editing (lead). **Yongxue Zhang:** Conceptualization (equal); Methodology (equal); Project administration (equal); Resources (equal); Supervision (equal); Writing – review & editing (equal). **Wenbo Zhou:** Conceptualization (supporting); Methodology (supporting); Writing – review & editing (supporting). **Cong Wang:** Conceptualization (supporting); Methodology (supporting); Writing – review & editing (supporting).

DATA AVAILABILITY

The data that support the findings of this study are available from the corresponding author upon reasonable request.

REFERENCES

[1]G. Lu, Z. Zuo, D. Liu, and S. Liu, "Energy balance and local unsteady loss analysis of flows in a low specific speed model pump-turbine in the positive slope region on the pump performance curve," Energies **12**, 1829 (2019).
[2]F. J. Lugauer, J. Kainz, and M. Gaderer, "Techno-economic efficiency analysis of various operating strategies for micro-hydro storage using a pump as a turbine," Energies **14**, 425 (2021).
[3]S. V. Jain and R. N. Patel, "Investigations on pump running in turbine mode: A review of the state-of-the-art," Renewable Sustainable Energy Rev. **30**, 841 (2014).
[4]N. Mousavi, G. Kothapalli, D. Habibi, C. K. Das, and A. Baniasadi, "A novel photovoltaic-pumped hydro storage microgrid applicable to rural areas," Appl. Energy **262**, 114284 (2020).
[5]S. Deniz, A. Del Rio, M. von Burg, and M. Tiefenthaler, "Investigation of the flow instabilities of a low specific speed pump turbine part 1: Experimental and numerical analysis," J. Fluids Eng. Trans. ASME **144**, 071209 (2022).
[6]B. Qian, J. Chen, P. Wu, D. Wu, P. Yan, and S. Li, "Investigation on inner flow quality assessment of centrifugal pump based on Euler head and entropy production analysis," IOP Conf. Ser. **240**, 092001 (2019).
[7]D. Li, H. Wang, Y. Qin, Z. Li, X. Wei, and D. Qin, "Mechanism of high amplitude low frequency fluctuations in a pump-turbine in pump mode," Renewable Energy **126**, 668 (2018).
[8]T. Xin, J. Wei, L. Qiuying, G. Hou, Z. Ning, W. Yuchuan, and C. Diyi, "Analysis of hydraulic loss of the centrifugal pump as turbine based on internal flow feature and entropy generation theory," Sustainable Energy Technol. Assess. **52**, 102070 (2022).
[9]M. M. Ghorani, M. H. Sotoude Haghighi, A. Maleki, and A. Riasi, "A numerical study on mechanisms of energy dissipation in a pump as turbine (PAT) using entropy generation theory," Renewable Energy **162**, 1036 (2020).
[10]G. Cavazzini, J. Houdeline, G. Pavesi, O. Teller, and G. Ardizzon, "Unstable behaviour of pump-turbines and its effects on power regulation capacity of pumped-hydro energy storage plants," Renewable Sustainable Energy Rev. **94**, 399 (2018).
[11]J. C. Hunt, A. A. Wray, and P. Moin, "Eddies, streams, and convergence zones in turbulent flows," in Studying Turbulence Using Numerical Simulation Databases, 2. Proceedings of the 1988 Summer Program (1988).
[12]J. Jeong and F. Hussain, "On the identification of a vortex," J. Fluid Mech. **285**, 69 (1995).
[13]L. ChaoQun, W. YiQian, Y. Yong, and D. ZhiWei, "New omega vortex identification method," Sci. China: Phys. Mech. Astron. **62**, 684711 (2016).
[14]Y. Gao and C. Liu, "Rortex and comparison with eigenvalue-based vortex identification criteria," Phys. Fluids **30**, 085107 (2018).
[15]C. Liu, Y. Gao, X. Dong, Y. Wang, J. Liu, Y. Zhang, X. Cai, and N. Gui, "Third generation of vortex identification methods: Omega and Liutex/Rortex based systems," J. Hydrodyn. **31**, 205 (2019).
[16]C. Liu, Y. Gao, S. Tian, and X. Dong, "Rortex—A new vortex vector definition and vorticity tensor and vector decompositions," Phys. Fluids **30**, 035103 (2018).
[17]Y. Wang, Y. Gao, J. Liu, and C. Liu, "Explicit formula for the Liutex vector and physical meaning of vorticity based on the Liutex-Shear decomposition," J. Hydrodyn. **31**, 464 (2019).
[18]C. Wang, Y. Zeng, Z. Yao, and F. Wang, "Rigid vorticity transport equation and its application to vortical structure evolution analysis in hydro-energy machinery," Eng. Appl. Comput. Fluid Mech. **15**, 1016 (2021).
[19]Y. Wang, H. Yu, W. Zhao, and D. Wan, "Liutex-based vortex control with implications for cavitation suppression," J. Hydrodyn. **33**, 74 (2021).
[20]W. Zhao, Y. Wang, S. Chen, C. Ma, and D. Wan, "Parametric study of Liutex-based force field models," J. Hydrodyn. **33**, 86 (2021).
[21]H. Hou, Y. Zhang, Z. Li, T. Jiang, J. Zhang, and C. Xu, "Numerical analysis of entropy production on a LNG cryogenic submerged pump," J. Nat. Gas Sci. Eng. **36**, 87 (2016).
[22]C. Wang, Y. Zhang, H. Hou, J. Zhang, and C. Xu, "Entropy production diagnostic analysis of energy consumption for cavitation flow in a two-stage LNG cryogenic submerged pump," Int. J. Heat Mass Transfer **129**, 342 (2019).
[23]C. Wang, Y. Zhang, Z. Liu, and Z. Yuan, "Multi-objective optimization of a two-stage liquefied natural gas cryogenic submerged pump-turbine in pump mode to reduce flow loss and cavitation," J. Energy Storage **52**, 105064 (2022).
[24]Z. Yuan, Y. Zhang, J. Zhang, and J. Zhu, "Experimental studies of unsteady cavitation at the tongue of a pump-turbine in pump mode," Renewable Energy **177**, 1265 (2021).
[25]Z. Yuan, Y. Zhang, C. Wang, and B. Lu, "Study on characteristics of vortex structures and irreversible losses in the centrifugal pump," Proc. Inst. Mech. Eng., Part A **235**, 1080 (2021).
[26]Y. Zhao and R. D. Sandberg, "Using a new entropy loss analysis to assess the accuracy of RANS predictions of an high-pressure turbine vane," J. Turbomach. **142**, 081008 (2020).
[27]H. Herwig and F. Kock, "Direct and indirect methods of calculating entropy generation rates in turbulent convective heat transfer problems," Heat Mass Transfer **43**, 207 (2006).

[28]H. Schlichting and J. Kestin, *Boundary Layer Theory* (Springer, 1961).
[29]P. Bradshaw and J. B. Perot, "A note on turbulent energy dissipation in the viscous wall region," Phys. Fluids A **5**, 3305 (1993).
[30]D. Lin, X. Yuan, and X. Su, "Local entropy generation in compressible flow through a high pressure turbine with delayed detached eddy simulation," Entropy **19**, 29 (2017).
[31]J. Liu and C. Liu, "Modified normalized Rortex/vortex identification method," Phys. Fluids **31**, 061704 (2019).
[32]X. Dong, S. Tian, and C. Liu, "Correlation analysis on volume vorticity and vortex in late boundary layer transition," Phys. Fluids **30**, 014105 (2018).
[33]I. B. Celik, U. Ghia, P. J. Roache, and C. J. Freitas, "Procedure for estimation and reporting of uncertainty due to discretization in CFD applications," J. Fluids Eng. Trans. ASME **130**, 078001 (2008).
[34]H. Alemi Arani, M. Fathi, M. Raisee, and S. A. Nourbakhsh, "The effect of tongue geometry on pump performance in reverse mode: An experimental study," Renewable Energy **141**, 717 (2019).